Composites Part B 118 (2017) 41–53

Contents lists available at ScienceDirect

Composites Part B

journal homepage: www.elsevier.com/locate/compositesb

Thermal response of ceramic matrix nanocomposite cylindrical shells using Eshelby-Mori-Tanaka homogenization scheme

B. Sobhaniaragh [a, *], R.C. Batra [b], W.J. Mansur [c, d], F.C. Peters [c, d]

[a] Young Researchers and Elite Club, Arak Branch, Islamic Azad University, Arak, Iran
[b] Department of Biomedical Engineering and Mechanics, Virginia Polytechnic Institute and State University, Blacksburg, VA 24061, USA
[c] Modelling Methods in Engineering and Geophysics Laboratory (LAMEMO), COPPE, Federal University of Rio de Janeiro, 21941-596, RJ, Brazil
[d] Department of Civil Engineering, COPPE, Federal University of Rio de Janeiro, RJ, Brazil

ARTICLE INFO

Article history:
Received 10 December 2016
Received in revised form
5 February 2017
Accepted 19 February 2017
Available online 8 March 2017

Keywords:
Ceramic-matrix composite
Carbon nanotubes
Two-parameter Eshelby-Mori-Tanaka scheme
Temperature-dependent properties
Sigmoidal power-law distribution
Third-order shear deformation theory

ABSTRACT

We find thermal stresses developed in Ceramic Matrix Composite (CMC) cylindrical shells reinforced with aggregated Carbon Nanotubes (CNTs) with heat flux prescribed on the inner surface and temperature on the outer surface. Null surface tractions are prescribed on these two surfaces and the cylinder edges are clamped. The material properties are homogenized by using a two-parameter Eshelby-Mori-Tanaka (EMT) approach. Material properties of the ceramic are assumed to depend upon the temperature, and the smooth variation of the CNT volume fraction through the shell thickness is assumed to be described either by a sigmoidal function or profile-O or profile-X often used in the literature. The one-way coupled thermo-mechanical problem is analyzed by first numerically solving the nonlinear heat equation with the Generalized Differential Quadrature Method (GDQM), and then the linear mechanical problem by using Reddy's Third-order Shear Deformation Theory (TSDT) and the GDQM. For the same thermal boundary conditions and the volume fraction of CNTs, the maximum hoop, the in-plane shear and the transverse normal stresses developed in the cylinder are highest for the profile-X of CNTs. The aggregation factor noticeably influences the maximum transverse normal and the maximum hoop stresses developed in the cylinder.

1. Introduction

The outstanding mechanical properties of Carbon Nano-Tubes (CNTs) make them unique candidates for reinforcing polymer, ceramic and metal matrix composites [1]. Whereas there has been a flurry of activity in studying mechanical properties of CNT-reinforced polymer composites not much work has been done in studying CNTs-reinforced ceramic composites. The combination of extraordinary characteristics of CNTs with intrinsic advantages of ceramic materials such as thermal stability, high corrosion resistance, low mass density and electrical insulation can generate CNT-Ceramic Matrix Composites (CNT-CMCs) with desired functional and structural properties [2,3]. The potential of developing high-performance CNT-CMCs that can withstand high temperature, severe chemical environment, and wear is very appealing with applications in such diverse areas as gas turbines, aerospace components and automobiles. Recent investigations on CNT-CMCs for potential structural applications are described in Refs. [4–15].

Zhan et al. [11,12] fabricated fully dense nanocomposites comprised of CNTs and nanocrystalline alumina matrix by using spark-plasma sintering, and demonstrated that their electrical conductivity improved over that of pristine alumina. Furthermore, CNT-alumina matrix nanocomposites with enhanced hardness and fracture toughness were successfully fabricated by Mo et al. [13] by a sol-gel process followed by spark plasma sintering. Zhu et al. [14] prepared bulk alumina ceramic composites by adding 2 wt.% CNTs under an alternating current electric field. By using catalytic pyrolysis of acetylene gas with iron nitrate impregnated alumina, An et al. [15] prepared CNT-alumina composites by hot-pressing them and investigated their mechanical and tribological properties.

During the solution of thermo-mechanical problems for CNT-ceramic composites, one usually deduces their effective moduli by employing homogenization techniques such as the Extended Rule of Mixtures (ERM) [16–18] or the Eshelby-Mori-Tanaka (EMT)

* Corresponding author. Young Researchers and Elite Club, Arak Branch, Islamic Azad University, Arak, Iran
E-mail addresses: sobhaniaragh@coc.ufrj.br, behnamsobhani@yahoo.com (B. Sobhaniaragh).

http://dx.doi.org/10.1016/j.compositesb.2017.02.032
1359-8368/

[19–21] method. Shen [16] modified the conventional rule of mixtures by introducing CNT efficiency parameters that were determined by matching the elastic moduli of polymer-based nanocomposites from molecular dynamics simulation results and the rule of mixtures. The ERM's limitations include disregarding intrinsic features, such as aggregation and waviness, of CNTs dispersed in the matrix. The EMT is based on the equivalent elastic inclusion concept of Eshelby [22] and the technique for estimating the average stress in the matrix phase proposed by Mori and Tanaka [23]. The EMT has been applied to CNT-Reinforced Composites (CNTRCs) by Odegard et al. [19] and has been improved upon by using test data [24–27] to account for the degree of the CNT aggregation, orientations, curviness and length. The Scanning Electron Microscopy (SEM) images [28,29] show that CNTs aggregate in a nanocomposite and form local regions of CNTs-concentration higher than their average volume fraction in the nanocomposite. Considering the CNT aggregation effects in the EMT model, Sobhaniaragh et al. [21,30] investigated natural frequencies and bending deformations of the CNTRC shells; e.g., see Sobhaniaragh's PhD thesis [31]. Furthermore, this methodology has been followed by Fantuzzi et al. [32], Kamarian et al. [33], Tornabene et al. [34], and Heshmati [35] for studying effects of agglomeration and distributions of CNTs on free vibration characteristics of CNT-nanocomposites.

Meguid and Sun [36] have experimentally shown that mechanical properties of CNTRCs deteriorate if the volume fraction of CNTs scattered within the matrix phase exceeds a limiting value. Thus, a designer should consider this limiting value of the CNT volume fraction for fulfilling multi-functional requirements. A possibility is to smoothly vary the volume fractions of CNTs and thus fabricate Functionally Graded Materials (FGMs) to economically achieve the desired multifunctionality. In recent years, several researchers have implemented the idea of smooth gradation of spatial CNT volume fraction in modeling nanocomposite structures to achieve desired structural response. For example, a large number of papers [21,32–35,37–46] have been devoted to studying vibrational characteristics of FG CNTRCs. The bending, buckling and postbuckling deformations of such structures have been studied in Refs. [30,46–52], and the thermal response of FG CNTRCs has been studied in Ref. [53]. Using the piezo-electricity theory and the ERM, Alibeigloo [53] studied thermo-elastic deformations of simply supported CNTRC cylindrical panel integrated with piezoelectric layers. With the temperature prescribed on the inner and the outer surfaces of the panel, the author concluded that the maximum radial stress as well as the axial and the circumferential displacements could be reduced by having a higher concentration of CNTs near the outer surface.

Motivated by the lack of research activity on thermal analysis of ceramic matrix nanocomposites reinforced by aggregated CNTs, we study here thermo-elastic response of CNT-CMC cylindrical shells subjected only to heat flux and temperature loads. A two-parameter EMT homogenization technique is employed that accounts for aggregation of CNTs in the ceramic matrix phase, and material properties of the ceramic matrix are assumed to be temperature-dependent. Consequently, the effective mechanical properties of CNTRCs are a function of both temperature and position, leading to nonlinear differential equations that cannot be analytically solved. The analysis of the mechanical problem is simplified by using Reddy's Third-order Shear Deformation Theory (TSDT) [54] with five unknowns. The nonlinear heat equation and the TSDT equations are numerically solved by employing the two-dimensional Generalized Differential Quadrature Method (GDQM) proposed by Shu [55] that has been shown to provide reasonably accurate solutions [56]. The smooth through-the-thickness spatial variation of CNTs volume fraction is characterized by a sigmoidal power-law distribution and two other distributions used in the literature [37,53].

2. Problem description

Consider a CNT-CMC cylindrical shell of finite length L, mean radius α_{3m}, and thickness h. As depicted in Fig. 1, we use global cylindrical coordinate axes $(\alpha_1, \alpha_2, \alpha_3)$ with the origin at the mid-surface of the left edge to label a material point of the cylinder in the unstressed reference configuration. The α_1-, the α_2- and the α_3-axes are, respectively, along the cylinder length, the

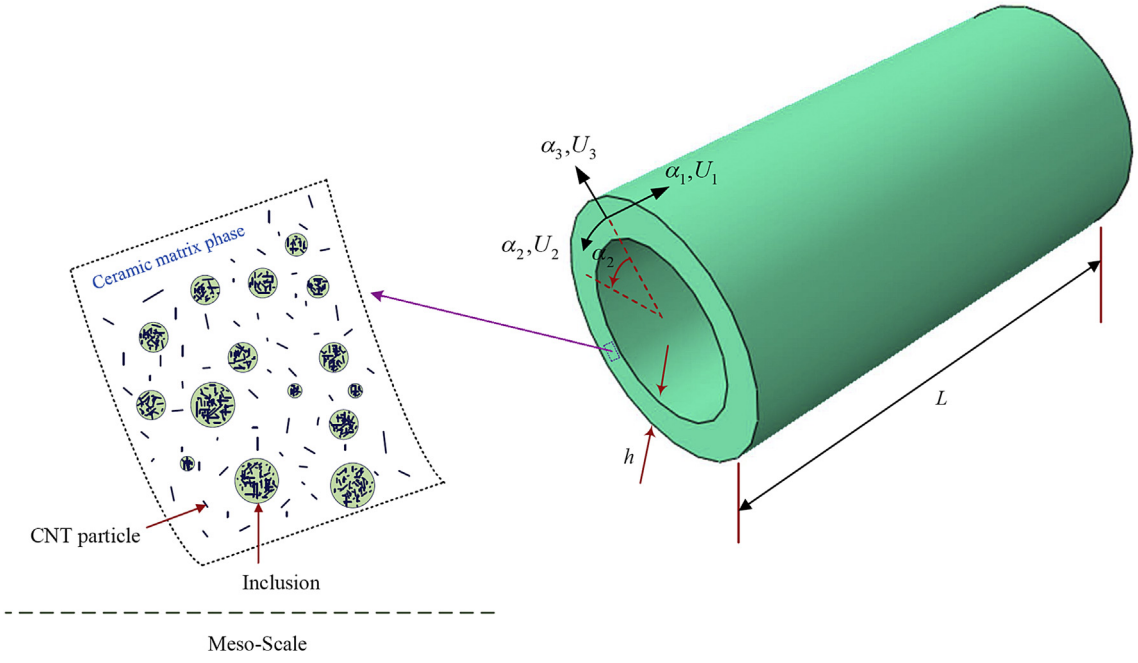

Fig. 1. Geometry of a CMC cylindrical shell reinforced by aggregated CNTs.

circumferential direction, and the cylinder thickness.

2.1. Two-parameter Eshelby-Mori-Tanaka (EMT) model

We briefly review a two-parameter EMT model for finding effective mechanical properties of CNT-CMCs. This homogenization scheme is based on Eshelby's theory [22] of elastic inclusions. Eshelby's results for a single inclusion in a semi-infinite elastic, isotropic and homogeneous medium are extended by the Mori-Tanaka method [23] to capture effects of numerous inhomogeneities embedded in a finite domain. Due to low bending stiffness and weak van der Waals forces [29], CNTs dispersed in CNT-CMCs aggregate in some regions resulting in a higher accumulation of CNTs there as compared to their average volume fraction in the entire CNT-CMCs. The regions with accumulated CNTs are assumed to be spherical and envisioned as inclusions that have material properties different from those of the material surrounding them. Hence, CNTs dispersed in the matrix are sorted according to their positions, i.e., embedded either inside or outside the inclusions, as depicted in Fig. 1. According to the two-parameter EMT model, the total volume V_r of the reinforcing phase is divided into two different parts [24]:

$$V_r = V_r^{inc} + V_r^m \tag{1}$$

with V_r^{inc} and V_r^m denoting, respectively, the volume of CNTs embedded in the inclusions (aggregated CNTs) and that dispersed in the matrix. The aggregation of CNTs in the ceramic matrix degrades its mechanical properties as compared to that of the virgin matrix. This aspect of the CNT-CMCs is described by introducing the aggregation parameters, ζ and ξ, defined as

$$\zeta = \frac{V^{inc}}{V}, \quad \xi = \frac{V_r^{inc}}{V_r} \tag{2}$$

where V^{inc} is the effective volume of the inclusions, and the parameter ζ equals the volume fraction of inclusions relative to the volume V of the representative volume element. For $\zeta = 1$, there is no aggregation of CNTs in the matrix phase, and for $0 < \zeta < 1$ the degree of aggregation of CNTs decreases with an increase in ζ. The parameter ξ equals the ratio of the CNTs volume embedded in the inclusions to the total volume of the CNTs. Thus for all CNTs accumulated in the inclusions, $\xi = 1$. For the CNTs to aggregate

$$\xi > \zeta \tag{3}$$

In order to predict the effective elastic moduli of the inclusions and the matrix phase, it is assumed that the volume fraction of CNTs varies only in the thickness direction. Furthermore, the CNTs are assumed to be transversely isotropic and randomly oriented in the spherical inclusions. Whereas some authors have assumed the axis of transverse isotropy to be along the CNT centroidal axis, Batra and Sears [57] have postulated it to be a radial line. The effective bulk modulus $K_{in}(\alpha_3)$ and the effective shear modulus $G_{in}(\alpha_3)$ of the spherical inclusions are given by [24,31,40]

$$K_{in}(\alpha_3) = K_m + \frac{f_r(\alpha_3)\xi(\delta_r - 3K_m\alpha_r)}{3(\zeta - f_r(\alpha_3)\xi + f_r(\alpha_3)\xi\alpha_r)} \tag{4}$$

$$G_{in}(\alpha_3) = G_m + \frac{f_r(a_3)\xi(\eta_r - 2G_m\beta_r)}{2(\zeta - f_r(\alpha_3)\xi + f_r(\alpha_3)\xi\alpha_r)} \tag{5}$$

Similarly, the effective bulk modulus $K_{out}(\alpha_3)$ and the effective shear modulus $G_{out}(\alpha_3)$ of the material outside the inclusions are given by

$$K_{out}(\alpha_3) = K_m + \frac{f_r(\alpha_3)(1-\xi)(\delta_r - 3K_m\alpha_r)}{3(1-\zeta - f_r(\alpha_3)(1-\xi) + f_r(\alpha_3)(1-\xi)\alpha_r)} \tag{6}$$

$$G_{out}(\alpha_3) = G_m + \frac{f_r(\alpha_3)(1-\xi)(\eta_r - 2G_m\beta_r)}{2(1-\zeta - f_r(\alpha_3)(1-\xi) + f_r(\alpha_3)(1-\xi)\beta_r)} \tag{7}$$

In Eqs. (4)–(7) K_m and G_m, respectively, denote the bulk and the shear moduli of the matrix;$f_r(\alpha_3)$ and $f_m(\alpha_3)$ with $f_r(\alpha_3) + f_m(\alpha_3) = 1$, respectively, denote volume fractions of the reinforcing and the matrix phases. Parameters α_r,β_r,δ_r, and η_r are defined by

$$\alpha_r = \frac{3(K_m + G_m) + k_r + l_r}{3(G_m + k_r)} \tag{8}$$

$$\beta_r = \frac{1}{5}\left[\frac{4G_m + 2k_r + l_r}{3(G_m + k_r)} + \frac{4G_m}{G_m + p_r} + \frac{2[G_m(3K_m + G_m) + G_m(3K_m + 7G_m)]}{G_m(3K_m + G_m) + m_r(3K_m + 7G_m)}\right] \tag{9}$$

$$\delta_r = \frac{1}{3}\left[n_r + 2l_r + \frac{(2k_r + l_r)(3K_m + 2G_m - l_r)}{G_m + k_r}\right] \tag{10}$$

$$\eta_r = \frac{1}{5}\left[\frac{2}{3}(n_r - l_r) + \frac{8G_m p_r}{G_m + p_r} + \frac{(2k_r - l_r)(2G_m + l_r)}{3(G_m + k_r)} + \frac{8m_r G_m(3K_m + 4G_m)}{3K_m(m_r + G_m) + G_m(7m_r + G_m)}\right] \tag{11}$$

in which k_r, m_r, n_r and l_r are Hill's elastic moduli for the CNTs [58,59].

The effective bulk modulus $K(\alpha_3)$ and the effective shear modulus $G(\alpha_3)$ of the CNT-CMCs are given by

$$K(\alpha_3) = K_{out}(\alpha_3)\left[1 + \frac{\zeta\left(\frac{K_{in}(\alpha_3)}{K_{out}(\alpha_3)} - 1\right)}{1 + d^0(\alpha_3)(1-\zeta)\left(\frac{K_{in}(\alpha_3)}{K_{out}(\alpha_3)} - 1\right)}\right] \tag{12}$$

$$G(\alpha_3) = G_{out}(\alpha_3)\left[1 + \frac{\zeta\left(\frac{G_{in}(\alpha_3)}{G_{out}(\alpha_3)} - 1\right)}{1 + \beta(\alpha_3)(1-\zeta)\left(\frac{G_{in}(\alpha_3)}{G_{out}(\alpha_3)} - 1\right)}\right] \tag{13}$$

where

$$d^0(\alpha_3) = \frac{1 + \nu_{out}(\alpha_3)}{3(1 - \nu_{out}(\alpha_3))} \tag{14}$$

$$\beta(\alpha_3) = \frac{2(4 - 5\nu_{out}(\alpha_3))}{3(1 - \nu_{out}(\alpha_3))} \tag{15}$$

The Poisson's ratio, $\nu_{out}(\alpha_3)$, of the matrix phase is given by

$$\nu_{out}(\alpha_3) = \frac{3K_{out}(\alpha_3) - 2G_{out}(\alpha_3)}{2[3K_{out}(\alpha_3) + G_{out}(\alpha_3)]} \tag{16}$$

We assume the CNT-CMC to be isotropic [24] and find its effective Young's modulus $E(\alpha_3)$ and Poisson's ratio $\nu(\alpha_3)$ from the following relations

$$E(\alpha_3) = \frac{9K(\alpha_3)G(\alpha_3)}{3K(\alpha_3) + G(\alpha_3)} \tag{17}$$

$$\nu(\alpha_3) = \frac{3K(\alpha_3) - 2G(\alpha_3)}{6K(\alpha_3) + 2G(\alpha_3)} \tag{18}$$

Furthermore, the thermal expansion coefficient, α, is calculated by Ref. [47].

$$\alpha(\alpha_3) = \frac{f_r(\alpha_3)E_r\alpha_r + f_m(\alpha_3)E_m\alpha_m}{f_r(\alpha_3)E_r + f_m(\alpha_3)E_m} \tag{19}$$

where α_r and α_m are the thermal expansion coefficients of the CNTs and the matrix, respectively. The thermal conductivity, $k(\alpha_3)$, of the CNC-CMT is expressed as [60,61].

$$k(\alpha_3) = \left(1 + \frac{qf_r(\alpha_3)}{3}\frac{k_r}{k_m(2a_k/d + q + k_r/k_m)}\right)k_m \tag{20}$$

where α_k is the Kapitza radius, k_m and k_r are thermal conductivities of the matrix and the reinforcing phases, respectively, d and l ($q = l/d$) are the diameter and the length of the CNTs, respectively.

We note that $f_r(\alpha_3) = V^*_{CNT}V_{CNT}(\alpha_3)$ where $V_{CNT}(\alpha_3)$ equals the CNT distribution through the shell's thickness, and V^*_{CNT} is the volume fraction of CNTs [62] given by

$$V^*_{CNT} = \left[\frac{\rho_{CNT}}{w_{CNT}\rho_m} - \frac{\rho_{CNT}}{\rho_m} + 1\right]^{-1} \tag{21}$$

where ρ_{CNT} and ρ_m equal, respectively, the mass densities of the CNTs and the matrix, and w_{CNT} equals the mass fraction of the CNTs.

Here we have assumed that the CNT volume fraction is given by the following sigmoidal power-law distribution

$$V_{CNT}(\alpha_3) = \left(\frac{e^{s\tilde{r}} - 1}{(e^{s/2} - 1)(e^{s(\tilde{r}-0.5)} + 1)}\right)^{\gamma} \tag{22}$$

in which $\tilde{r} = (\alpha_3 + h/2)/h$, the sigmoid exponent s and the parameter γ control the CNT-variation profile in the radial (or the thickness) direction as depicted in Fig. 2. The inner surface of the shell with the heat flux prescribed has lower CNT volume fraction that should alleviate thermal stresses and provide desired structural response. With an increase in the value of s, the continuously graded shell approaches a laminated shell with two lamina having CNT volume fractions of 0 and V^*_{CNT} on the inner and the outer surfaces, respectively. Here, we compute results for CNT profiles often used by others [21,37,53] as well as for profile-X and profile-O. It was reported in Ref. [21] that the CNT volume fractions symmetrically distributed about the shell midsurface are more effective in reducing (increasing) the natural frequency than the uniform (asymmetric) distributions.

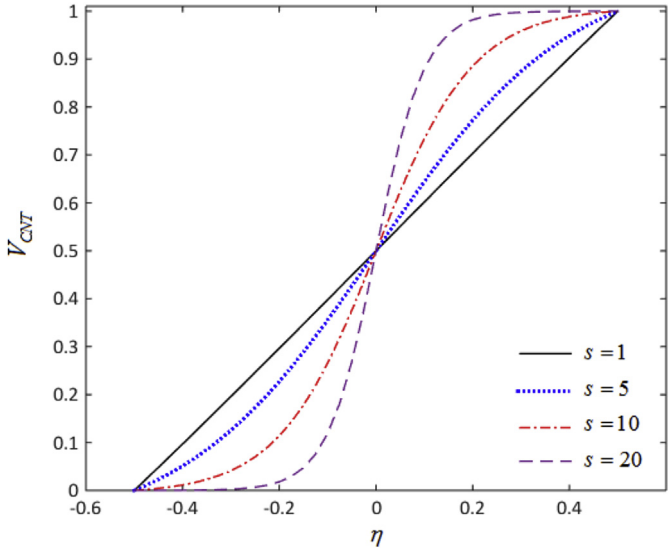

Fig. 2. Through-the-thickness distribution of the CNT volume fraction for various values of the sigmoid exponent, s, when $\gamma = 1$.

2.2. Temperature-dependent material properties

It is anticipated that continuously graded CNT-CMCs studied in this paper will be used in high temperature environments and material properties of the ceramic phase are expected to be temperature dependent. Accordingly, we consider the temperature dependence of mechanical properties of the CNT-CMC, and assume that Young's modulus E, the thermal conductivity k, and the thermal expansion coefficient α (denoted by P in Eq. (23)) are given by

$$P(T) = P_0\left(P_{-1}T^{-1} + 1 + P_1T + P_2T^2 + P_3T^3\right) \tag{23}$$

where P_0, P_{-1}, P_1, P_2 and P_3 are constants whose values for Alumina as the ceramic matrix are taken from Refs. [13,63].

2.3. Third-Order Shell Theory (TSDT)

Based on Reddy's [54] TSDT in which straight lines normal to the shell mid-surface before deformation do not necessarily remain straight during the deformation, the following displacement field is assumed:

$$\begin{aligned} U_1 &= u_1(\alpha_1,\alpha_2) + \alpha_3\phi_1(\alpha_1,\alpha_2) - C{\alpha_3}^3\left(\phi_1 + \frac{\partial u_3}{\partial \alpha_1}\right) \\ U_2 &= u_2(\alpha_1,\alpha_2) + \alpha_3\phi_2(\alpha_1,\alpha_2) + C{\alpha_3}^3\left(\frac{u_2}{\alpha_{3m}} - \phi_2 - \frac{1}{\alpha_{3m}}\frac{\partial u_3}{\partial \alpha_2}\right) \\ U_3 &= u_3(\alpha_1,\alpha_2) \end{aligned} \tag{24}$$

where $C = 4/3h^2$, and U_1, U_2 and U_3 are displacement components, respectively, along the α_1-, the α_2- and the α_3- axes. Substituting from Eq. (25) into the strain-displacement relations [64] gives

$$\begin{aligned} \varepsilon_{11} &= \varepsilon^0_{11} + \alpha_3\varepsilon'_{11} + {\alpha_3}^2\varepsilon''_{11} + {\alpha_3}^3\varepsilon'''_{11} \\ \varepsilon_{22} &= \varepsilon^0_{22} + \alpha_3\varepsilon'_{22} + {\alpha_3}^2\varepsilon''_{22} + {\alpha_3}^3\varepsilon'''_{22} \\ \varepsilon_{12} &= \varepsilon^0_{12} + \alpha_3\varepsilon'_{12} + {\alpha_3}^2\varepsilon''_{12} + {\alpha_3}^3\varepsilon'''_{12} \\ \varepsilon_{13} &= \varepsilon^0_{13} + \alpha_3\varepsilon'_{13} + {\alpha_3}^2\varepsilon''_{13} + {\alpha_3}^3\varepsilon'''_{13} \\ \varepsilon_{23} &= \varepsilon^0_{23} + \alpha_3\varepsilon'_{23} + {\alpha_3}^2\varepsilon''_{23} + {\alpha_3}^3\varepsilon'''_{23} \end{aligned} \tag{25}$$

where

$$\begin{aligned} &\varepsilon^0_{11} = u_{1,1}, \quad \varepsilon'_{11} = \phi_{1,1}, \quad \varepsilon''_{11} = 0, \quad \varepsilon'''_{11} = -C(\phi_{1,1} + u_{3,11}) \\ &\varepsilon^0_{22} = (1/\alpha_{3m})u_{2,2} + u_3/\alpha_{3m}, \quad \varepsilon'_{22} = (1/\alpha_{3m})\phi_{2,2}, \quad \varepsilon''_{22} = 0 \\ &\varepsilon''_{22} = C((1/\alpha_{3m})u_{2,2} - (1/\alpha_{3m})\phi_{2,2} - (1/\alpha_{3m})u_{3,22}) \\ &\varepsilon^0_{12} = (1/\alpha_{3m})u_{1,2} + u_{2,1}, \quad \varepsilon'_{12} = (1/\alpha_{3m})\phi_{1,2} + \phi_{2,1} \quad \varepsilon''_{12} = 0 \\ &\varepsilon'''_{12} = -(C/\alpha_{3m})\phi_{1,2} - (C/\alpha_{3m})u_{3,12} + (C/\alpha_{3m})u_{2,1} - C\phi_{2,1} \\ &\varepsilon^0_{13} = \phi_1 + u_{3,1}, \quad \varepsilon'_{13} = 0, \quad \varepsilon''_{13} = -3C(\phi_1 + w_{,1}) \\ &\varepsilon'''_{13} = 0, \quad \varepsilon^0_{23} = \phi_2 + (1/\alpha_{3m})u_{3,1}, \quad \varepsilon'_{23} = 0 \\ &\varepsilon''_{23} = 3C(-(1/\alpha_{3m})u_{3,2} - \phi_2 + (u_2/\alpha_{3m})), \quad \varepsilon'''_{23} = 0 \end{aligned} \tag{26}$$

Setting $\sigma_{33}=0$ in Hooke's law for infinitesimal thermo-elastic deformations, solving it for ε_{33}, and substituting for ε_{33} in Hooke's law for 3-dimensional deformations, the reduced constitutive relation for the cylindrical shell is given by

$$\begin{bmatrix}\sigma_{11}\\ \sigma_{22}\\ \sigma_{12}\\ \sigma_{13}\\ \sigma_{23}\end{bmatrix}=\begin{bmatrix}Q_{11} & Q_{12} & 0 & 0 & 0\\ Q_{12} & Q_{22} & 0 & 0 & 0\\ 0 & 0 & Q_{66} & 0 & 0\\ 0 & 0 & 0 & Q_{44} & 0\\ 0 & 0 & 0 & 0 & Q_{55}\end{bmatrix}\begin{bmatrix}\varepsilon_{11}\\ \varepsilon_{22}\\ \varepsilon_{12}\\ \varepsilon_{13}\\ \varepsilon_{23}\end{bmatrix}-\begin{bmatrix}\beta_{11}\\ \beta_{22}\\ 0\\ 0\\ 0\end{bmatrix}T \tag{27}$$

where $[Q]$ is the matrix of material elasticities, β_i the stress moduli for the thermal expansion coefficients [64], and T the change in temperature from that in the stress-free reference configuration. Expressions for the forces and the moments for the shell are given by

$$\begin{Bmatrix}N_{11}\\ N_{22}\\ N_{12}\end{Bmatrix}=\int_{-h/2}^{h/2}\begin{Bmatrix}\sigma_{11}\\ \sigma_{22}\\ \sigma_{12}\end{Bmatrix}d\alpha_3,\qquad \begin{Bmatrix}M_{11}\\ M_{22}\\ M_{12}\end{Bmatrix}=\int_{-h/2}^{h/2}\begin{Bmatrix}\sigma_{11}\\ \sigma_{22}\\ \sigma_{12}\end{Bmatrix}\alpha_3 d\alpha_3, \tag{28}$$

$$\begin{Bmatrix}P_{11}\\ P_{22}\\ P_{12}\end{Bmatrix}=\int_{-h/2}^{h/2}\begin{Bmatrix}\sigma_{11}\\ \sigma_{22}\\ \sigma_{12}\end{Bmatrix}{\alpha_3}^3 d\alpha_3,\qquad \begin{Bmatrix}P_{13}\\ P_{23}\end{Bmatrix}=\int_{-h/2}^{h/2}\begin{Bmatrix}\sigma_{13}\\ \sigma_{23}\end{Bmatrix}{\alpha_3}^3 d\alpha_3$$

$$\begin{Bmatrix}Q_{13}\\ Q_{23}\end{Bmatrix}=\int_{-h/2}^{h/2}\begin{Bmatrix}\sigma_{13}\\ \sigma_{23}\end{Bmatrix}d\alpha_3,\qquad \begin{Bmatrix}R_{13}\\ R_{23}\end{Bmatrix}=\int_{-h/2}^{h/2}\begin{Bmatrix}\sigma_{13}\\ \sigma_{23}\end{Bmatrix}{\alpha_3}^2 d\alpha_3 \tag{29}$$

Substituting from Eqs. (26) and (27) into Eqs. (28) and (29) gives

$$\begin{aligned}
N_{11}&=A_{10}\varepsilon^0_{11}+A_{11}\varepsilon'_{11}+A_{12}\varepsilon''_{11}+A_{13}\varepsilon'''_{11}+T_{10}\\
N_{22}&=A_{10}\varepsilon^0_{22}+A_{11}\varepsilon'_{22}+A_{12}\varepsilon''_{22}+A_{13}\varepsilon'''_{22}+T_{20}\\
N_{12}&=B_{10}\varepsilon^0_{12}+B_{11}\varepsilon'_{12}+B_{12}\varepsilon''_{12}+B_{13}\varepsilon'''_{12}\\
M_{11}&=A_{11}\varepsilon^0_{11}+A_{12}\varepsilon'_{11}+A_{13}\varepsilon''_{11}+A_{14}\varepsilon'''_{11}+T_{11}\\
M_{22}&=A_{11}\varepsilon^0_{22}+A_{12}\varepsilon'_{22}+A_{13}\varepsilon''_{22}+A_{14}\varepsilon'''_{22}+T_{11}\\
M_{12}&=B_{11}\varepsilon^0_{12}+B_{12}\varepsilon'_{12}+B_{13}\varepsilon''_{12}+B_{14}\varepsilon'''_{12}\\
P_{11}&=A_{13}\varepsilon^0_{11}+A_{14}\varepsilon'_{11}+A_{15}\varepsilon''_{11}+A_{16}\varepsilon'''_{11}+T_{13}\\
P_{22}&=A_{13}\varepsilon^0_{22}+A_{14}\varepsilon'_{22}+A_{15}\varepsilon''_{22}+A_{16}\varepsilon'''_{22}+T_{23}\\
P_{12}&=B_{13}\varepsilon^0_{12}+B_{14}\varepsilon'_{12}+B_{15}\varepsilon''_{12}+B_{16}\varepsilon'''_{12}\\
P_{13}&=B_{13}\varepsilon^0_{13}+B_{14}\varepsilon'_{13}+B_{15}\varepsilon''_{13}+B_{16}\varepsilon'''_{13}\\
P_{23}&=B_{13}\varepsilon^0_{23}+B_{14}\varepsilon'_{23}+B_{15}\varepsilon''_{23}+B_{16}\varepsilon'''_{23}\\
Q_{13}&=B_{10}\varepsilon^0_{13}+B_{11}\varepsilon'_{13}+B_{12}\varepsilon''_{13}+B_{13}\varepsilon'''_{13}\\
Q_{23}&=B_{10}\varepsilon^0_{23}+B_{11}\varepsilon'_{23}+B_{12}\varepsilon''_{23}+B_{13}\varepsilon'''_{23}\\
R_{13}&=B_{12}\varepsilon^0_{13}+B_{13}\varepsilon'_{13}+B_{14}\varepsilon''_{13}+B_{15}\varepsilon'''_{13}\\
R_{23}&=B_{12}\varepsilon^0_{23}+B_{13}\varepsilon'_{23}+B_{14}\varepsilon''_{23}+B_{15}\varepsilon'''_{23}
\end{aligned} \tag{30}$$

in which

$$A_{10}=\int_{-h/2}^{h/2}\frac{E(\alpha_3,T)}{1-\nu^2}d\alpha_3,\quad A_{11}=\int_{-h/2}^{h/2}\frac{E(\alpha_3,T)\alpha_3}{1-\nu^2}d\alpha_3,\quad A_{12}=\int_{-h/2}^{h/2}\frac{E(\alpha_3,T){\alpha_3}^2}{1-\nu^2}d\alpha_3,$$

$$A_{13}=\int_{-h/2}^{h/2}\frac{E(\alpha_3,T){\alpha_3}^3}{1-\nu^2}d\alpha_3,\quad T_{10}=-\int_{-h/2}^{h/2}\frac{E(\alpha_3,T)\beta_{11}T}{1-\nu^2}d\alpha_3,\quad T_{11}=-\int_{-h/2}^{h/2}\frac{E(\alpha_3,T)\alpha_3\beta_{11}T}{1-\nu^2}d\alpha_3,$$

$$T_{13}=-\int_{-h/2}^{h/2}\frac{E(\alpha_3,T){\alpha_3}^3\beta_{11}T}{1-\nu^2}d\alpha_3,\quad B_{10}=\int_{-h/2}^{h/2}\frac{E(\alpha_3,T)}{2(1+\nu)}d\alpha_3,\quad B_{11}=\int_{-h/2}^{h/2}\frac{E(\alpha_3,T)\alpha_3}{2(1+\nu)}d\alpha_3,$$

$$B_{12}=\int_{-h/2}^{h/2}\frac{E(\alpha_3,T){\alpha_3}^2}{2(1+\nu)}d\alpha_3,\quad B_{13}=\int_{-h/2}^{h/2}\frac{E(\alpha_3,T){\alpha_3}^3}{2(1+\nu)}d\alpha_3,\quad B_{14}=\int_{-h/2}^{h/2}\frac{E(\alpha_3,T){\alpha_3}^4}{2(1+\nu)}d\alpha_3,$$

$$B_{15}=\int_{-h/2}^{h/2}\frac{E(\alpha_3,T){\alpha_3}^5}{2(1+\nu)}d\alpha_3,\quad B_{16}=\int_{-h/2}^{h/2}\frac{E(\alpha_3,T){\alpha_3}^6}{2(1+\nu)}d\alpha_3,\quad T_{20}=-\int_{-h/2}^{h/2}\frac{E(\alpha_3,T)\beta_{22}T}{1-\nu^2}d\alpha_3,$$

$$T_{11} = -\int_{-h/2}^{h/2} \frac{E(\alpha_3,T)\beta_{22}T}{1-\nu^2}d\alpha_3, \quad T_{23} = -\int_{-h/2}^{h/2} \frac{E(\alpha_3,T)\beta_{22}\alpha_3{}^3T}{1-\nu^2}d\alpha_3 \tag{31}$$

Equations governing infinitesimal deformations of the thermo-elastic shell can be written as follows:

$$\frac{\alpha_{3m}\partial N_{11}}{\partial\alpha_1} - \frac{\partial N_{12}}{\partial\alpha_2} = 0$$
$$\frac{\partial N_{22}}{\partial\alpha_2} + \frac{\alpha_{3m}\partial N_{12}}{\partial\alpha_1} + Q_{23} + \frac{C}{\alpha_{3m}}\frac{\partial P_{22}}{\partial\alpha_2} + C\frac{\partial P_{12}}{\partial\alpha_1} - 3CR_{23} - \frac{C}{\alpha_{3m}}P_{23} = 0$$
$$-C\alpha_{3m}\frac{\partial^2 P_{11}}{\partial\alpha_1{}^2} + N_{22} - \frac{C}{\alpha_{3m}}\frac{\partial^2 P_{22}}{\partial\alpha_2{}^2} - C\frac{\partial^2 P_{12}}{\partial\alpha_1\partial\alpha_2} - \alpha_{3m}\frac{\partial Q_{23}}{\partial\alpha_1} + 3C\alpha_{3m}\frac{\partial R_{13}}{\partial\alpha_1} - \frac{\partial Q_{23}}{\partial\alpha_2} + 3C\frac{\partial R_{23}}{\partial\alpha_2} - \frac{C}{\alpha_{3m}}\frac{\partial P_{23}}{\partial\alpha_2} = 0$$
$$\frac{\alpha_{3m}\partial M_{11}}{\partial\alpha_1} - C\alpha_{3m}\frac{\partial P_{11}}{\partial x} + \frac{\partial M_{12}}{\partial\alpha_2} - C\frac{\partial P_{12}}{\partial\alpha_2} + 3CR_{13} - \alpha_{3m}Q_{13} = 0$$
$$\frac{\partial M_{22}}{\partial\alpha_2} + C\frac{\partial P_{22}}{\partial\alpha_2} - \partial\alpha_1\frac{\partial M_{12}}{\partial\alpha_1} + C\alpha_{3m}\frac{\partial P_{12}}{\partial\alpha_1} + \alpha_{3m}\left(Q_{23} - 3CQ_{23} - 2C\frac{1}{\alpha_{3m}}P_{23}\right) = 0 \tag{32}$$

Here we consider shells with edges $\alpha_1 = 0$, L clamped, and the inner and the outer surfaces $\alpha_3 = h/2, -h/2$ traction free. In order to further simplify the problem, we assume the displacement field to have the following series expansion:

$$\begin{Bmatrix} u_1 \\ u_2 \\ u_3 \\ \phi_1 \\ \phi_2 \end{Bmatrix} = \sum_{n=1}^{\infty} \begin{Bmatrix} \overline{u}_{1n}(\alpha_1)\cos(n\alpha_2) \\ \overline{u}_{2n}(\alpha_1)\sin(n\alpha_2) \\ \overline{u}_{3n}(\alpha_1)\cos(n\alpha_2) \\ \overline{\phi}_{1n}(\alpha_1)\cos(n\alpha_2) \\ \overline{\phi}_{2n}(\alpha_1)\sin(n\alpha_2) \end{Bmatrix} \tag{33}$$

While solving the mechanical problem, the temperature field is assumed to be known.

The 3-dimensional steady-state heat conduction equation in the absence of heat sources can be stated as [65]

$$\frac{\partial k}{\partial\alpha_3}\frac{\partial T}{\partial\alpha_3} + k\frac{\partial^2 T}{\partial\alpha_3{}^2} + \left(\frac{\alpha_{3m}}{\alpha_{3m}+\alpha_3}\right)^2 k\frac{\partial T^2}{\partial\alpha_2{}^2} + \frac{\partial k}{\partial\alpha_1}\frac{\partial T}{\partial\alpha_1} + k\frac{\partial^2 T}{\partial\alpha_1{}^2} + \frac{1}{\alpha_{3m}+\alpha_3}k\frac{\partial T}{\partial\alpha_3} = 0 \tag{34}$$

Because of the dependence of the thermal conductivity $k(\alpha_3, T)$ upon the temperature, Eq. (34) is non-linear in T. Thermal boundary conditions considered in this work are:

$$\text{Heat convection at } \alpha_1 = 0: \quad k(\alpha_3,T)\frac{\partial T}{\partial\alpha_1} + h_a(T - T_\infty) = 0 \tag{35}$$

$$\text{Heat convection at } \alpha_1 = L: \quad k(\alpha_3,T)\frac{\partial T}{\partial\alpha_1} + h_a(T - T_\infty) = 0 \tag{36}$$

$$\text{Temperature prescribed at } \alpha_3 = h/2: \quad T = T_0 \tag{37}$$

$$\text{Heat flux prescribed at } \alpha_3 = -h/2: \quad q = q_{flux} \tag{38}$$

In Eqs. (35) and (36), $T_\infty = 300K$ equals the temperature of the ambient air, and h_a the convective heat transfer coefficient, and we set $T_0 = 523$K.

3. Numerical solution

The one-way coupled thermo-mechanical problem is analyzed by first solving nonlinear Eq. (34) for the temperature field and then analyzing the linear mechanical problem. Equation (34) is numerically solved by the GDQM-based iterative procedure.

3.1. Thermal problem

The temperature field is assumed to be given by

$$T(\alpha_1,\alpha_2,\alpha_3) = \sum_{n=1}^{\infty} \mathrm{T}_n(\alpha_1,\alpha_3)\sin(n\alpha_2) \tag{39}$$

Substitution from Eq. (39) into Eq. (34) results in an equation that involves partial derivatives of T_n with respect to α_1 and α_3. These are approximated in terms of the values of T_n at discrete points by the GDQM [31,55] as follows

$$\left.\frac{\partial^r f(\varsigma)}{\partial\varsigma^r}\right|_{(\varsigma=\varsigma_i)} = \sum_{k=1}^{N_\varsigma} c_{ik}^{(r)} f(\varsigma_k), \quad i = 1,2,\ldots,N_\varsigma \tag{40}$$

Here N_ς denotes the number of grid points and $c_{ij}^{(r)}$ the corresponding weights given by the following recursive relations for the first-order derivative, i.e., $r = 1$.

$$c_{ij}^{(1)} = \frac{L^{(1)}(\varsigma_i)}{(\varsigma_i - \varsigma_j)L^{(1)}(\varsigma_j)}, \qquad i,j = 1,2,\ldots,N_\varsigma, \quad i \neq j \tag{41}$$

where

$$L^{(1)}(\varsigma_i) = \prod_{j=1, i\neq j}^{N_\varsigma} (\varsigma_i - \varsigma_j), \tag{42}$$

The weighting coefficients for the higher-order derivatives are derived by the following iterative relations.

$$c_{ij}^{(r)} = r\left(c_{ii}^{(r-1)}c_{ij}^{(1)} - \frac{c_{ij}^{(r-1)}}{(\varsigma_i - \varsigma_j)}\right), \qquad i,j = 1,2,\ldots,N_\varsigma, \quad i \neq j \quad r = 2,3,,\ldots N_\varsigma - 1 \tag{43}$$

$$c_{ii}^{(r)} = -\sum_{j=1, i\neq j}^{N_\varsigma} c_{ij}^{(r)}, \qquad i = 1,2,\ldots,N_\varsigma, \quad r = 1,2,\ldots N_\varsigma - 1 \tag{44}$$

We employ the Chebyshev-Gauss-Lobatto (CGL) quadrature points given by Ref. [40]

$$\varsigma_i = \frac{1}{2}\left(1 - \cos\left(\frac{i-1}{N_\varsigma - 1}\pi\right)\right), \qquad i = 1,2,\ldots,N_\varsigma \tag{45}$$

as the grid points. As reported in a number of papers including [55,56] the use of these non-uniformly distributed sampling points yields results of good accuracy. We note that Eq. (40) is similar to that obtained by using the smooth symmetric hydrodynamics basis functions, e.g., see Refs. [66,67].

The discrete form of Eqs. (34)–(38) can be written in the following compact form

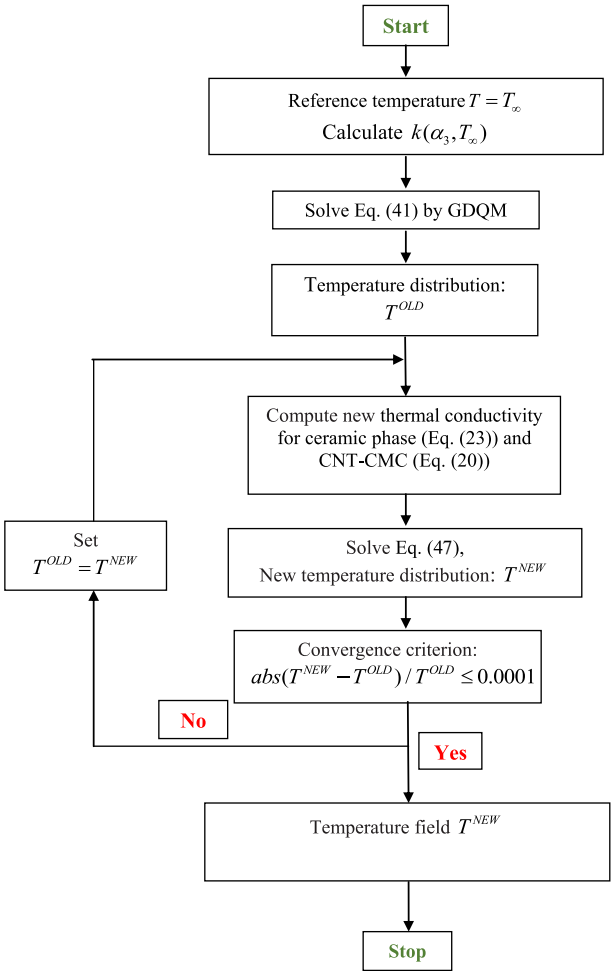

Fig. 3. Flow chart for iterative solution procedure of non-linear heat transfer equation.

$$\begin{bmatrix} [A_{bb}] & [A_{bd}] \\ [A_{db}] & [A_{dd}] \end{bmatrix} \begin{Bmatrix} \mathrm{T}_b \\ \mathrm{T}_d \end{Bmatrix} = \begin{Bmatrix} \{f_C\} \\ \{0\} \end{Bmatrix} \tag{46}$$

where subscripts '*d*' and '*b*' denote the domain and the boundary points, respectively, and the vector $\{f_C\}$ includes terms due to heat convection conditions prescribed at $\alpha_1 = 0$ and $\alpha_1 = L$. By condensation of the boundary degrees of freedom, the temperatures at the domain grid points are given by

$$\{\mathrm{T}_d\} = [B]^{-1}[A_{db}][A_{bb}]^{-1}\{f_C\} \tag{47}$$

where

$$[B] = [A_{db}][A_{bb}]^{-1}[A_{bd}] - [A_{dd}] \tag{48}$$

Noted that Eq. (47) is non-linear in temperature due to the temperature-dependent thermal conductivity, $k(\alpha_3, T)$. It is iteratively solved with the procedure described in the flow chart of Fig. 3.

3.2. Mechanical problem

With the temperature distribution known, equations for the mechanical problem are discretized by using the GDQM. Denoting degrees of freedom of the sampling points within and on the boundary of the domain by subscripts *d* and *b*, respectively, we arrive at the following set of linear algebraic equations.

$$\begin{bmatrix} [A_{bb}] & [A_{bd}] \\ [A_{db}] & [A_{dd}] \end{bmatrix} \begin{Bmatrix} \delta_b \\ \delta_d \end{Bmatrix} = \begin{Bmatrix} \{F_{Tb}\} \\ \{F_{Td}\} \end{Bmatrix} \tag{49}$$

Here $\{F_{Tb}\}$ and $\{F_{Td}\}$ are load vectors due to the temperature field. Similar to the solution technique for Eq. (46), we get

$$\{\delta_d\} = [L]^{-1}\left[\{F_{Td}\} - [A_{db}][A_{bb}]^{-1}\{F_{Tb}\}\right] \tag{50}$$

where

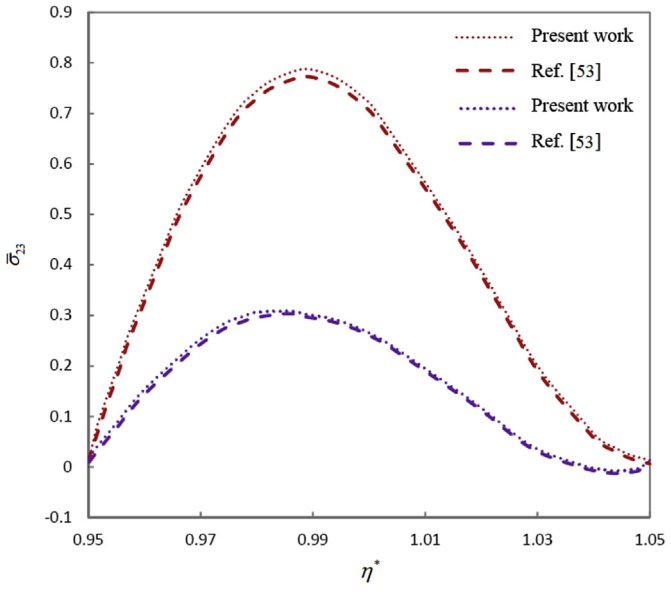

Fig. 4. Variation of the transverse shear stress through the thickness of CNT-reinforced cylindrical panel subjected to a thermal load (red and blue lines, respectively, correspond to $V_{CNT}^* = 0.17$ and 0.14). (For interpretation of the references to colour in this figure legend, the reader is referred to the web version of this article.)

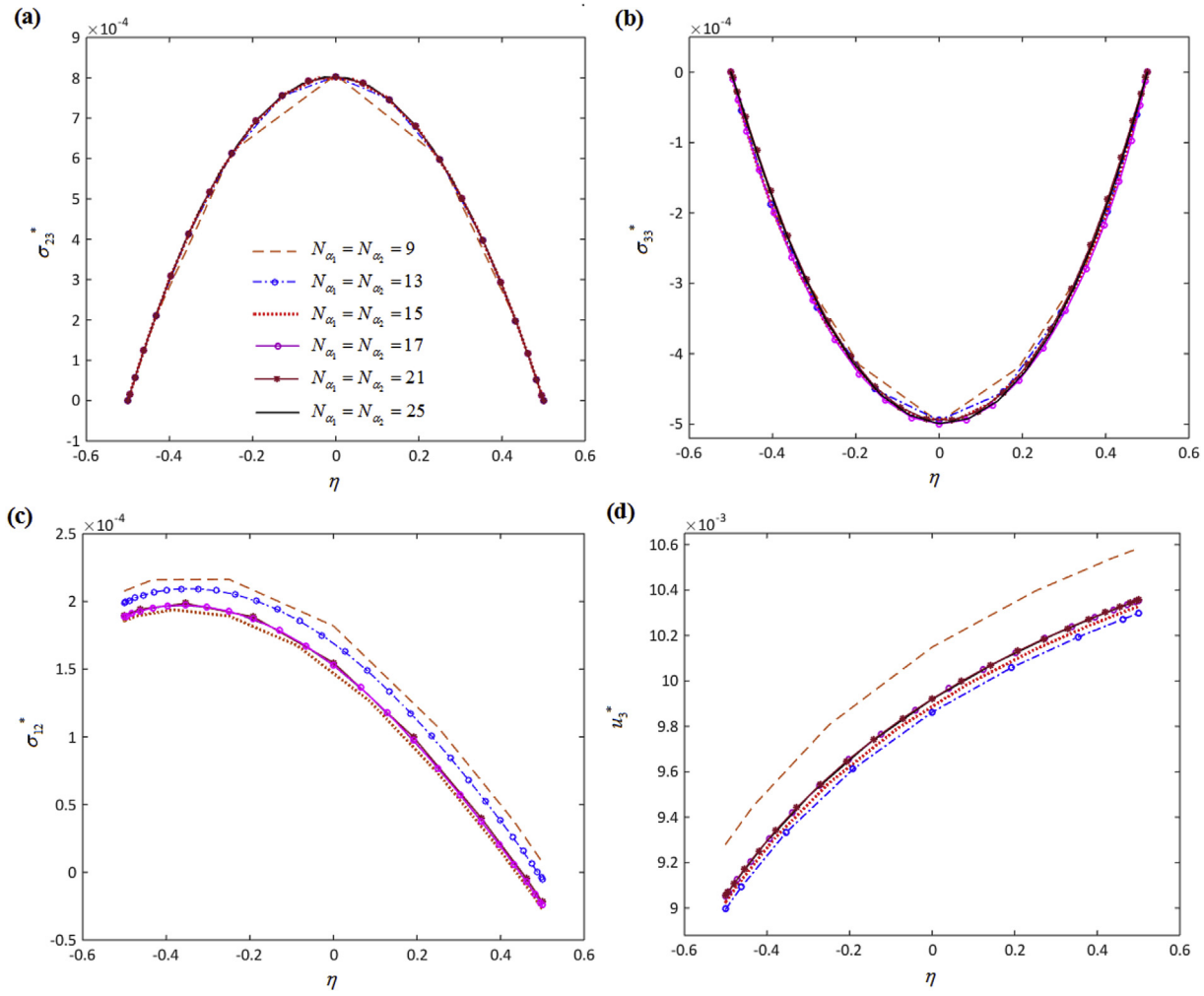

Fig. 5. Convergence of the through-the-thickness non-dimensional thermal stresses and the radial displacement in a linearly graded CNT-CMC cylindrical shell $\alpha_{3m}/h = 20,\ \gamma = 1,\ s = 1,\ \xi = 0.7,\ \zeta = 0.5$.

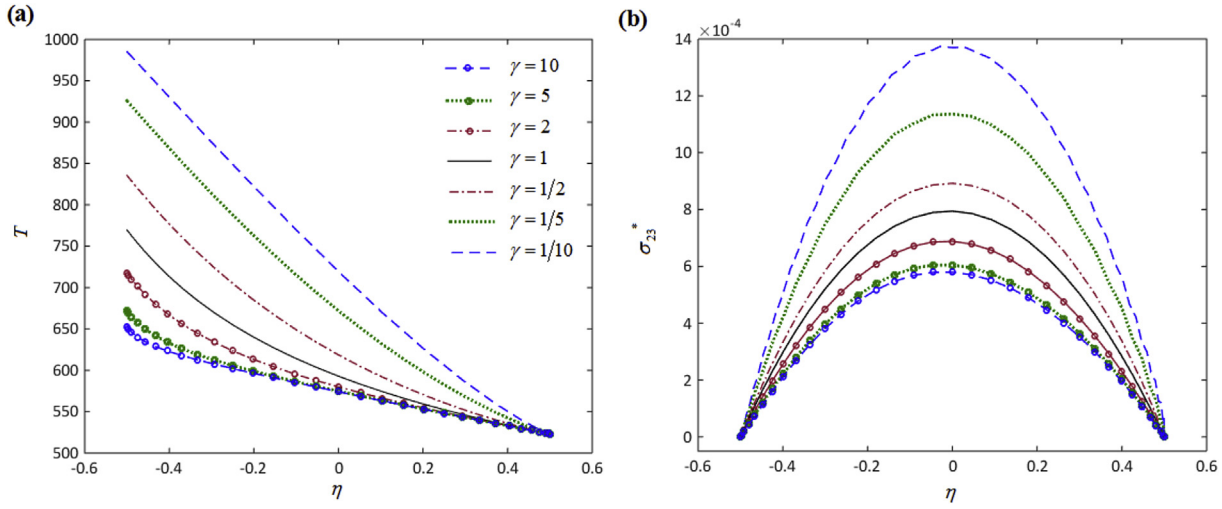

Fig. 6. Variation of the temperature field and the transverse shear stress in the CNT-CMC cylindrical shell for several values of the CNT volume fraction index $(\alpha_{3m}/h = 10,\ \alpha_1 = L/2,\ s = 1,\ \xi = 1)$.

$$[L] = [A_{dd}] - [A_{db}][A_{bb}]^{-1}[A_{bd}] \tag{51}$$

4. Results and discussion

In order to verify our computational algorithm, we compare computed results for the simply-supported cylindrical panel problem with those of Ref. [53] for the (10, 10) SWCNTs-polymer composite. In Ref. [53] the ERM homogenization technique is employed and following values are assigned to different variables:

$$\frac{\alpha_{3m}}{h} = 10, \quad h = 10\text{mm}, \quad \Theta = \frac{\pi}{3}, \quad \frac{L}{\alpha_{3m}} = 3 \tag{52}$$

Thermal and mechanical loads:

$$\text{at } \alpha_3 = h/2 :, \; T = T_0 \sin\left(\frac{\pi\alpha_2}{\Theta}\right), \; Q = Q_0 \sin\left(\frac{\pi\alpha_2}{\Theta}\right),$$

$$\text{at } \alpha_3 = -h/2 : \; T = T_1 \sin\left(\frac{\pi\alpha_2}{\Theta}\right), \; Q = 0 \tag{53}$$

Here Θ denotes the panel angle, $T_0 = 300$K and $T_1 = 273$K, and the Q_0 is peak value of the distributed surface traction applied on the outer surface of the shell. Following [53], we set $Q_0 = 2.1$ GPa. It is clear from results plotted in Fig. 4 that the presently computed transverse shear stress with $\zeta = 1$ (i.e., no aggression of CNTs in the matrix phase) and the EMT homogenization scheme agrees well with that reported in Fig. 3c of [53]; the nomenclature and the non-dimensionalization used are the same as in Ref. [53]. The magnitude of the transverse shear stress based on the EMT model is slightly higher than that based on the ERM approach. An increase in V^*_{CNT} from 0.14 to 0.17 increases the maximum transverse normal stress by a factor of about 3.

We report below through-the-thickness variations of the thermal stresses, displacements, and the temperature field for continuously graded and temperature-dependent CMC cylindrical shell reinforced with different volume fractions of aggregated CNTs and with clamped edges. Results are presented in terms of non-dimensional displacements and stresses denoted by an * and defined as (see [68])

$$(u_1^*, u_2^*, u_3^*) = \frac{k_m(u_1, u_2, u_3)}{\alpha_m L^2 q_o}, \sigma_i^* = \frac{k_m \sigma_i}{\alpha_m E_m L q_o} \tag{55}$$

Here α_m, k_m, and E_m are properties of the matrix phase of the nanocomposite and α_{3m} denotes the radius of the shell mid-surface. The geometrical parameters of the shell are $L = 0.7$m, $\alpha_{3m} = 0.3$m, the matrix material is Alumina with temperature-dependent properties borrowed from Refs. [13,63] and the reinforcements

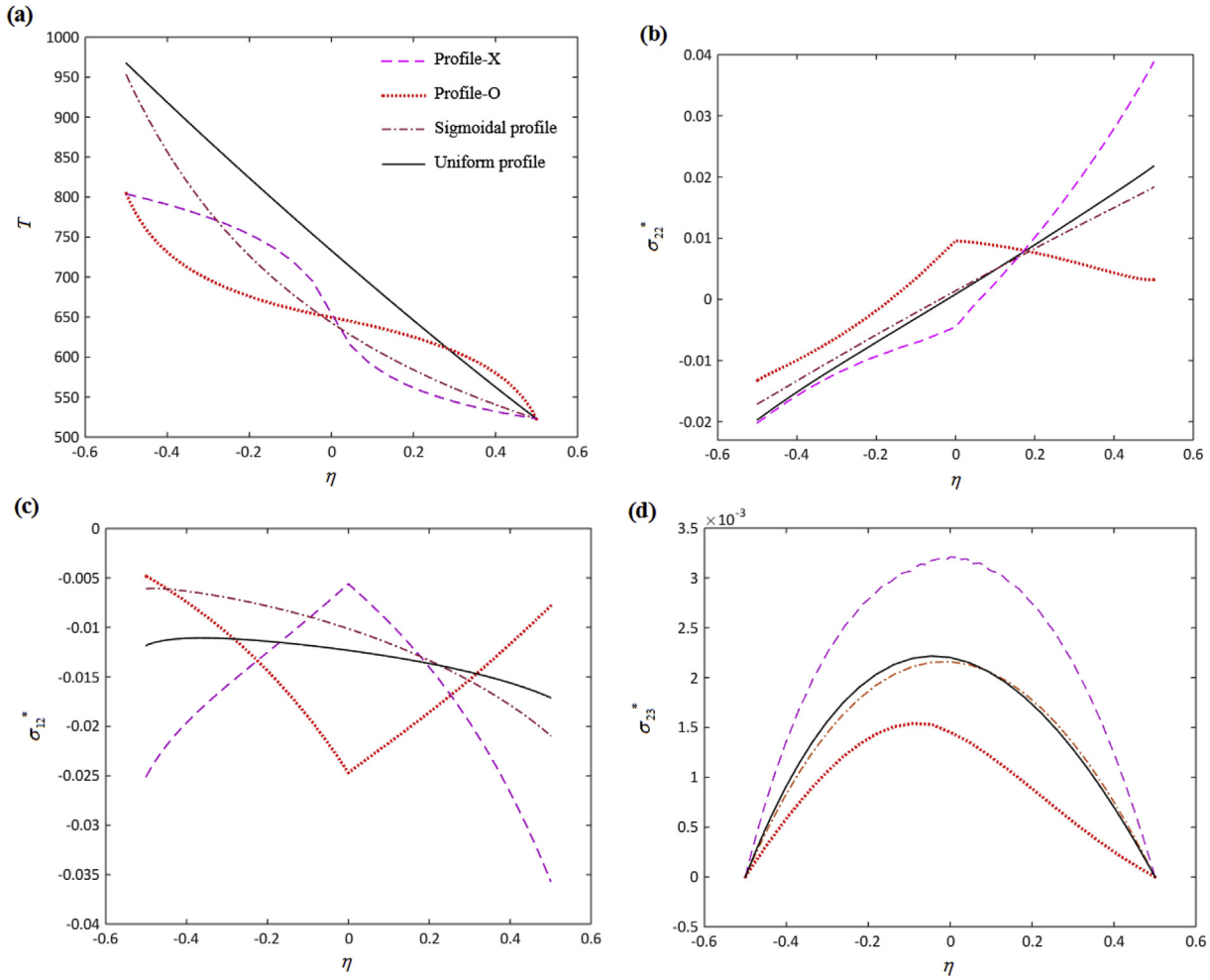

Fig. 7. Through-the-thickness distributions of the temperature, the circumferential and the transverse shear thermal stresses in a continuously graded CNT-CMC cylindrical shell for various CNT volume fraction profiles ($\alpha_{3m}/h = 5$, $\alpha_1 = L/2$, $\gamma = 1$, $s = 1$, $\xi = 1$).

are armchair (10, 10) SWCNTs [17] with $V^*_{CNT} = 0.17$ unless otherwise mentioned. In the parametric study provided in this section, the temperature is in Kelvin and the heat flux applied to the shell inner surface $q_o = 1E6$ W/m^{2}K [68]. The heat transfer coefficient of the air is assumed to be $h_a = 100$ W/m^{2}K. The shell thickness coordinate normalized by $h/2$ is denoted by η.

A convergence study of the through-the-thickness thermal stresses and the radial displacement is presented in Fig. 5 for the CNTs volume fraction corresponding to $s = 1, \gamma = 1$ in Eq. (22). These results evince that the solution obtained with the GDQM rapidly converges with an increase in the number of sampling points in the α_1 and the α_2 directions. The convergence of the transverse shear and the transverse normal stresses is faster than that of the in-plane shear stress and the radial displacement. The maximum values of the three stress components plotted in Fig. 5 are of the same order of magnitude.

In Fig. 6 we have exhibited the through-the-thickness variation of the temperature and the transverse shear stress for different values of γ in Eq. (22) for the CNTs volume fraction and $\xi = 1$, i.e., all CNTs are aggregated in the inclusions. The temperature gradient at the outer surface, $\eta = 0.5$, and the transverse shear stress at the mid-surface, $\eta = 0$, increase as the value of γ is increased from 1/10 to 10. The value of γ that minimizes σ_{23} at the shell mid-surface also gives the smallest temperature at the shell inner surface.

The effects of several CNT volume fraction profiles, namely X, O, sigmoidal and uniform [21,37,53], on the through-the-thickness distributions of the temperature, the circumferential or the hoop, and the transverse shear stresses are depicted in Fig. 7. The O and the sigmoidal profiles have no CNTs on the shell inner surface. The temperature on the shell inner surface is the lowest for the O and the X profiles and the highest for the uniform profile. The maximum value of the hoop stress is highest for the X profile and it occurs at the shell outer surface. For the O profile, the hoop stress has the maximum value at the shell mid-surface. For the O and the X profiles, the slope of the in-plane shear stress is discontinuous at the shell mid-surface. The four CNT profiles considered give qualitatively similar through-the-thickness distributions of the transverse shear stress with the O (X) profile giving the smallest (largest) value at the shell mid-surface.

The through-the-thickness variations of the temperature, the circumferential stress, and the out-of-plane transverse shear stresses for different values of s in Eq. (22) are shown in Fig. 8. With an increase in the value of s, the temperature gradient in going from the outer to the inner shell surface increases especially from the

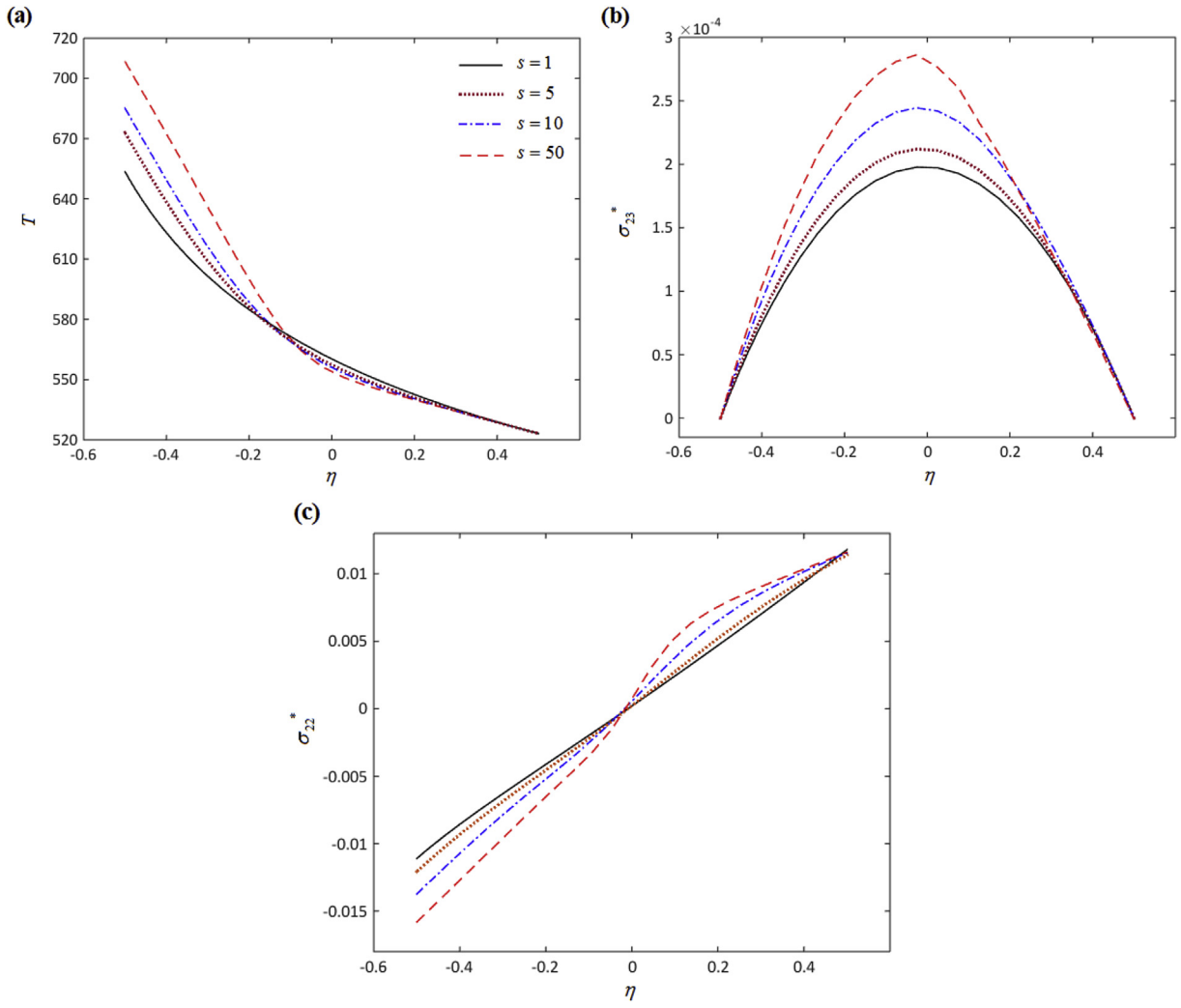

Fig. 8. Effect of values of the sigmoidal exponent on the through-the-thickness variations of the temperature and the circumferential and the transverse shear stresses ($\alpha_{3m}/h = 50,\ \alpha_1 = L/2,\ \gamma = 1,\ \xi = 1$).

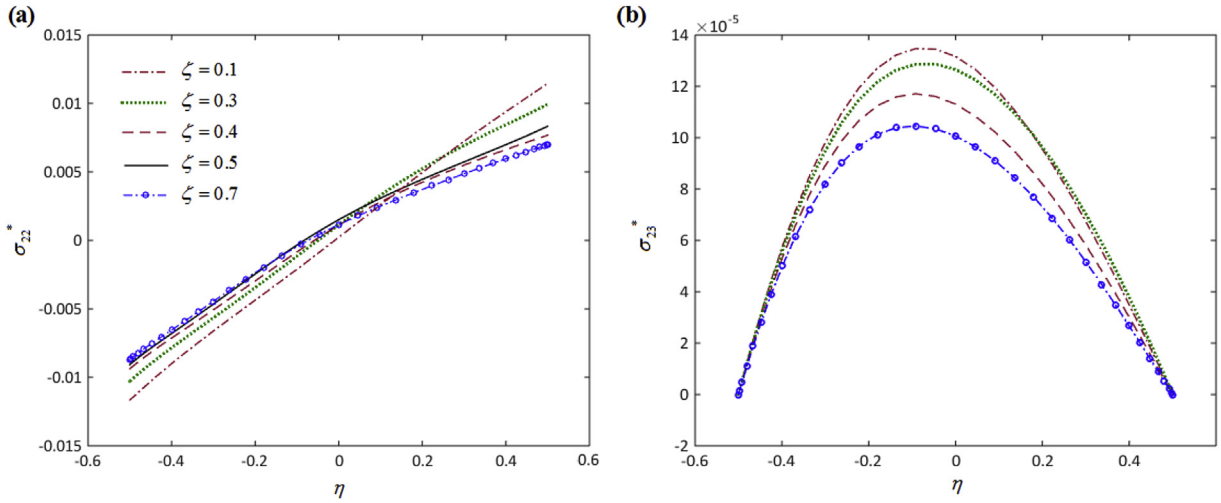

Fig. 9. Impact of aggregation parameter ζ on the transverse shear thermal stresses in a continuously graded CNT-CMC cylindrical shell ($\alpha_{3m}/h = 20,\ \alpha_1 = L/2,\ \gamma = 1,\ s = 1,\ \xi = 0.9$).

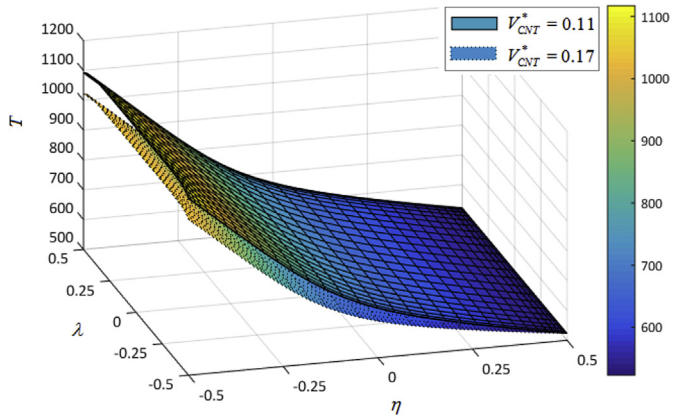

Fig. 10. Temperature field in a continuously graded CNT-CMC cylindrical shell for two volume fractions of CNTs ($\alpha_{3m}/h = 5,\ \alpha_1 = L/2,\ \gamma = 1,\ s = 10,\ \xi = 1$). Here λ is non-dimensional coordinate along the α_1-direction.

mid-surface to the inner surface, the maximum value of the transverse shear stress increases with an increase in the value of s and their qualitative distributions are nearly the same for $s = 1, 5, 10$ and 50. We note that an increase in the value of s results in lower volume fraction of CNTs at the shell inner surface. As shown in Fig. 2, for $s = 50$ we have a laminated shell with negligible (highest) volume fraction of CNTs on the inner (outer) one-half of the shell. This affects more through-the-thickness distribution of the transverse shear stress around the mid-surface than the temperature and the hoop stress distributions.

In Fig. 9 we have displayed through-the-thickness variations of the hoop and the transverse shear stress for the aggregation parameter $\zeta = 0.1$, 0.3, 0.4, 0.5 and 0.7. The hoop stress at the outer surface of the shell does not vary monotonically with the change in ζ. For volume fractions of the CNTs equal to 0.11 and 0.17, distributions of the temperature on the $\alpha_1\alpha_3$- plane are displayed in Fig. 10. It should be noted that the temperature is prescribed on the shell outer surface. These plots evince that increasing the CNT volume fraction from 0.11 to 0.17 decreases the maximum temperature induced from 1100 to 1020 K. The temperature in the axial direction, except at points near the end faces, is uniform because the material properties are independent of the α_1- coordinate.

5. Remarks

We note that the exact solution for thermoelastic deformations of rectangular plates is provided in [69] and a higher-order shear and normal deformable plate theory is used in [70] to analyze transient thermoelastic deformations. Finite deformations of curved beams considering both geometric and material non-linearities are studied in [71,72] using a third-order shear and normal deformable theory.

6. Conclusions

Thermal stresses induced in a CNT-reinforced ceramic matrix composite cylindrical shell with temperature-dependent material properties have been analyzed by first solving the nonlinear heat conduction equation and then the linear thermoelasticity equations by using Reddy's TSDT and the GDQM. The effective moduli have been deduced by using the Eshelby-Mori-Tanaka scheme considering the agglomeration of CNTs. The cylinder is clamped at the edges and its inner and outer surfaces are traction free. The temperature is prescribed on the outer surface and the heat flux on the inner surface. It is found that the thermal design of continuously graded CNTRCs using the widely assumed through-the-thickness CNT variations known as, profile-O and profile-X, give discontinuities at the shell mid-surface in slopes of the hoop and the in-plane shear stresses. Furthermore, for the profile-X the peak magnitude of the stresses is higher than that for other variations of the CNTs. The consideration of the aggregation of CNTs noticeably increases the maximum magnitudes of the in-plane thermal stresses.

Acknowledgments

The last two authors would like to acknowledge the CNPq (Brazilian Council for Scientific and Technological Development) with grant number of 306933/2014-4, and of the FAPERJ (Research Foundation of the State of Rio de Janeiro) with grant number of 203.234/2016.

References

[1] Bououdina M, editor. Handbook of research on nanoscience, nanotechnology, and advanced materials. IGI Global; 2014.
[2] Cho J, Boccaccini AR, Shaffer MS. Ceramic matrix composites containing

carbon nanotubes. J Mater Sci 2009 1;44(8):1934–51.
[3] Low IM, editor. Advances in ceramic matrix composites. Woodhead Publishing; 2014.
[4] Vasudevan S, Kothari A, Sheldon BW. Direct observation of toughening and R-curve behavior in carbon nanotube reinforced silicon nitride. Scr Mater 2016 Nov 30;124:112–6.
[5] Jambagi SC, Kar S, Brodard P, Bandyopadhyay PP. Characteristics of plasma sprayed coatings produced from carbon nanotube doped ceramic powder feedstock. Mater Des 2016 Dec 15;112:392–401.
[6] Jiang D, Thomson K, Kuntz JD, Ager JW, Mukherjee AK. Effect of sintering temperature on a single-wall carbon nanotube-toughened alumina-based nanocomposite. Scr Mater 2007 30;56(11):959–62.
[7] Yamamoto G, Omori M, Hashida T. Preparation of carbon nanotube-toughened alumina composites. In: Water dynamics, vol. 987; 2008 Feb. p. 83–5.
[8] Morisada Y, Miyamoto Y, Takaura Y, Hirota K, Tamari N. Mechanical properties of SiC composites incorporating SiC-coated multi-walled carbon nanotubes. Int J Refract Metals Hard Mater 2007 Jul 31;25(4):322–7.
[9] Sun J, Gao L, Li W. Colloidal processing of carbon nanotube/alumina composites. Chem Mater 2002 Dec 16;14(12):5169–72.
[10] Sun J, Gao L, Jin X. Reinforcement of alumina matrix with multi-walled carbon nanotubes. Ceram Int 2005 Dec 31;31(6):893–6.
[11] Zhan GD, Kuntz JD, Wan J, Mukherjee AK. Single-wall carbon nanotubes as attractive toughening agents in alumina-based nanocomposites. Nat Mater 2003 Jan 1;2(1):38–42.
[12] Zhan GD, Kuntz JD, Garay JE, Mukherjee AK. Electrical properties of nanoceramics reinforced with ropes of single-walled carbon nanotubes. Appl Phys Lett 2003;83(6):1228–30.
[13] Mo CB, Cha SI, Kim KT, Lee KH, Hong SH. Fabrication of carbon nanotube reinforced alumina matrix nanocomposite by sol–gel process. Mater Sci Eng A 2005 Mar 25;395(1):124–8.
[14] Zhu YF, Shi L, Zhang C, Yang XZ, Liang J. Preparation and properties of alumina composites modified by electric field-induced alignment of carbon nanotubes. Appl Phys A 2007 Nov 1;89(3):761–7.
[15] An JW, You DH, Lim DS. Tribological properties of hot-pressed alumina-CNT composites. Wear 2003 Sep 30;255(1):677–81.
[16] Shen HS. Nonlinear bending of functionally graded carbon nanotube-reinforced composite plates in thermal environments. Compos Struct 2009 Nov 30;91(1):9–19.
[17] Zhu P, Lei ZX, Liew KM. Static and free vibration analyses of carbon nanotube-reinforced composite plates using finite element method with first order shear deformation plate theory. Compos Struct 2012 Mar 31;94(4):1450–60.
[18] Zhang LW, Lei ZX, Liew KM. Buckling analysis of FG-CNT reinforced composite thick skew plates using an element-free approach. Compos Part B Eng 2015 Jun 15;75:36–46.
[19] Odegard GM, Gates TS, Wise KE, Park C, Siochi EJ. Constitutive modeling of nanotube–reinforced polymer composites. Compos Sci Technol 2003 Aug 31;63(11):1671–87.
[20] Formica G, Lacarbonara W, Alessi R. Vibrations of carbon nanotube-reinforced composites. J Sound Vib 2010 May 10;329(10):1875–89.
[21] Sobhaniaragh B, Barati AN, Hedayati H. Eshelby–Mori–Tanaka approach for vibrational behavior of continuously graded carbon nanotube-reinforced cylindrical panels. Compos Part B Eng 2012 Jun 30;43(4):1943–54.
[22] Eshelby JD. The determination of the elastic field of an ellipsoidal inclusion, and related problems. In: Proceedings of the royal society of London a: mathematical, physical and engineering sciences, vol. 241. The Royal Society; 1957 Aug 20. p. 376–96. No. 1226.
[23] Mori T, Tanaka K. Average stress in matrix and average elastic energy of materials with misfitting inclusions. Acta metall 1973 May 1;21(5):571–4.
[24] Shi DL, Feng XQ, Huang YY, Hwang KC, Gao H. The effect of nanotube waviness and agglomeration on the elastic property of carbon nanotube-reinforced composites. J Eng Mater Technol 2004 Jul 1;126(3):250–7.
[25] Formica G, Lacarbonara W. Three-dimensional modeling of interfacial stick-slip in carbon nanotube nanocomposites. Int J Plast 2017 Jan 31;88:204–17.
[26] Fisher FT, Bradshaw RD, Brinson LC. Fiber waviness in nanotube-reinforced polymer composites: modulus predictions using effective nanotube properties. Compos Sci Technol 2003 Aug 31;63(11):1689–703.
[27] Pan J, Bian L, Zhao H, Zhao Y. A new micromechanics model and effective elastic modulus of nanotube reinforced composites. Comput Mater Sci 2016 Feb 15;113:21–6.
[28] Talò M, Krause B, Pionteck J, Lanzara G, Lacarbonara W. An updated micromechanical model based on morphological characterization of carbon nanotube nanocomposites. Compos Part B Eng 2016 Oct 18 (In press).
[29] Gkikas G, Barkoula NM, Paipetis AS. Effect of dispersion conditions on the thermo-mechanical and toughness properties of multi walled carbon nanotubes-reinforced epoxy. Compos Part B Eng 2012 Sep 30;43(6):2697–705.
[30] Mehrabadi SJ, Sobhaniaragh B. Stress analysis of functionally graded open cylindrical shell reinforced by agglomerated carbon nanotubes. Thin-Walled Struct 2014 Jul 31;80:130–41.
[31] Sobhaniaragh B. Vibration and thermal stress analyses of functionally graded materials. Belgium: Ghent University; 2014. PhD dissertation.
[32] Fantuzzi N, Tornabene F, Bacciocchi M, Dimitri R. Free vibration analysis of arbitrarily shaped Functionally Graded Carbon Nanotube-reinforced plates. Compos Part B Eng 2016 Sep 10 (In press).
[33] Kamarian S, Salim M, Dimitri R, Tornabene F. Free vibration analysis of conical shells reinforced with agglomerated carbon nanotubes. Int J Mech Sci 2016;108:157–65.
[34] Tornabene F, Fantuzzi N, Bacciocchi M, Viola E. Effect of agglomeration on the natural frequencies of functionally graded carbon nanotube-reinforced laminated composite doubly-curved shells. Compos Part B Eng 2016;89:187–218.
[35] Heshmati M, Yas MH. Free vibration analysis of functionally graded CNT-reinforced nanocomposite beam using Eshelby-Mori-Tanaka approach. J Mech Sci Technol 2013;27(11):3403–8.
[36] Meguid SA, Sun Y. On the tensile and shear strength of nano-reinforced composite interfaces. Mater Des 2004 Jun 30;25(4):289–96.
[37] Song ZG, Zhang LW, Liew KM. Active vibration control of CNT-reinforced composite cylindrical shells via piezoelectric patches. Compos Struct 2016 Dec 15;158:92–100.
[38] Selim BA, Zhang LW, Liew KM. Vibration analysis of CNT reinforced functionally graded composite plates in a thermal environment based on Reddy's higher-order shear deformation theory. Compos Struct 2016 November 15;156:276–90.
[39] Ansari R, Torabi J, Shojaei MF. Vibrational analysis of functionally graded carbon nanotube-reinforced composite spherical shells resting on elastic foundation using the variational differential quadrature method. Eur J Mech-A/Solids 2016 Dec 31;60:166–82.
[40] Hedayati H, Sobhaniaragh B. Influence of graded agglomerated CNTs on vibration of CNT-reinforced annular sectorial plates resting on Pasternak foundation. Appl Math Comput 2012 May 1;218(17):8715–35.
[41] Sharma A, Kumar A, Susheel CK, Kumar R. Smart damping of functionally graded nanotube reinforced composite rectangular plates. Compos Struct 2016 Nov 1;155:29–44.
[42] Mehar K, Panda SK. Geometrical nonlinear free vibration analysis of FG-CNT reinforced composite flat panel under uniform thermal field. Compos Struct 2016 May 20;143:336–46.
[43] Wu HL, Yang J, Kitipornchai S. Nonlinear vibration of functionally graded carbon nanotube-reinforced composite beams with geometric imperfections. Compos Part B Eng 2016 Apr 1;90:86–96.
[44] Wang ZX, Shen HS. Nonlinear dynamic response of nanotube-reinforced composite plates resting on elastic foundations in thermal environments. Nonlinear Dyn 2012 Oct 1;70(1):735–54.
[45] Phung-Van P, Abdel-Wahab M, Liew KM, Bordas SP, Nguyen-Xuan H. Isogeometric analysis of functionally graded carbon nanotube-reinforced composite plates using higher-order shear deformation theory. Compos Struct 2015 May 31;123:137–49.
[46] Sobhaniaragh B, Farahani EB, Barati AN. Natural frequency analysis of continuously graded carbon nanotube-reinforced cylindrical shells based on third-order shear deformation theory. Math Mech Solids 2013 May 1;18(3):264–84.
[47] Shen HS. Thermal buckling and postbuckling behavior of functionally graded carbon nanotube-reinforced composite cylindrical shells. Compos Part B Eng 2012 30;43(3):1030–8.
[48] Zhang LW, Liew KM, Reddy JN. Postbuckling of carbon nanotube reinforced functionally graded plates with edges elastically restrained against translation and rotation under axial compression. Comput Methods Appl Mech Eng 2016 Jan 1;298:1–28.
[49] Mehrabadi SJ, Sobhaniaragh B, Khoshkhahesh V, Taherpour A. Mechanical buckling of nanocomposite rectangular plate reinforced by aligned and straight single-walled carbon nanotubes. Compos Part B Eng 2012 Jun 30;43(4):2031–40.
[50] Wang M, Li ZM, Qiao P. Semi-analytical solutions to buckling and free vibration analysis of carbon nanotube-reinforced composite thin plates. Compos Struct 2016 Jun 1;144:33–43.
[51] Wu H, Kitipornchai S, Yang J. Thermo-electro-mechanical postbuckling of piezoelectric FG-CNTRC beams with geometric imperfections. Smart Mater Struct 2016 Aug 9;25(9):095022.
[52] Sobhaniaragh B, Abdel Wahab M. Buckling of functionally graded carbon nanotube-fiber reinforced plates under mechanical loads. In: 3rd international journal of fracture fatigue and wear, vol. 2. Laboratory Soete–Ghent University; 2014. p. 148–54.
[53] Alibeigloo A. Elasticity solution of functionally graded carbon nanotube-reinforced composite cylindrical panel subjected to thermo mechanical load. Compos Part B Eng 2016 Feb 15;87:214–26.
[54] Reddy JN. A refined nonlinear theory of plates with transverse shear deformation. Int J Solids Struct 1984 Dec 31;20(9):881–96.
[55] Shu C. Differential quadrature and its application in engineering. Springer Science & Business Media; 2012.
[56] Tornabene F, Fantuzzi N, Ubertini F, Viola E. Strong formulation finite element method based on differential quadrature: a survey. Appl Mech Rev 2015 Mar 1;67(2):020801.
[57] Batra RC, Sears A. Uniform radial expansion/contraction of carbon nanotubes and their transverse elastic moduli. Model Simul Mater Sci Eng 2006;15:835–44.
[58] Cristescu ND, Craciun EM, Soós E. Mechanics of elastic composites. CRC Press; 2003.
[59] Hill RA. self-consistent mechanics of composite materials. J Mech Phys Solids 1965 Aug 31;13(4):213–22.
[60] Yang SY, Ma CC, Teng CC, Huang YW, Liao SH, Huang YL, et al. Effect of functionalized carbon nanotubes on the thermal conductivity of epoxy composites. Carbon 2010 Mar 31;48(3):592–603.

[61] Nan CW, Liu G, Lin Y, Li M. Interface effect on thermal conductivity of carbon nanotube composites. Appl Phys Lett 2004 Oct 18;85(16):3549–51.
[62] Fidelus JD, Wiesel E, Gojny FH, Schulte K, Wagner HD. Thermo-mechanical properties of randomly oriented carbon/epoxy nanocomposites. Compos Part A Appl Sci Manuf 2005 Nov 30;36(11):1555–61.
[63] Reddy JN, Chin CD. Thermo-mechanical analysis of functionally graded cylinders and plates. J Therm Stresses 1998 Sep 1;21(6):593–626.
[64] Reddy JN. Mechanics of laminated composite plates and shells: theory and analysis. CRC press; 2004.
[65] Pelletier JL, Vel SS. An exact solution for the steady-state thermoelastic response of functionally graded orthotropic cylindrical shells. Int J solids Struct 2006 31;43(5):1131–58.
[66] Batra RC, Zhang GM. SSPH basis functions for meshless methods, and comparison of solutions with strong and weak formulations. Comput Mech 2008;41:527–45.
[67] Zhang GM, Batra RC. Symmetric smoothed particle hydrodynamics (SSPH) method and its application to elastic problems. Comput Mech 2009;43:321–40.
[68] Vel SS, Batra RC. Three-dimensional analysis of transient thermal stresses in functionally graded plates. Int J Solids Struct 2003;40:7181–96.
[69] Vel SS, Batra RC. Exact solution for thermoelastic deformations of functionally graded thick rectangular plates. AIAA J 2002;40:1421–2.
[70] Qian LF, Batra RC. Transient thermoelastic deformations of a thick functionally graded plate. J Therm Stress 2004;27:705–40.
[71] Batra RC, Xiao J. Analysis of post-buckling and delamination in laminated composite St. Venant-Kirchhoff beams using CZM and layerwise TSNDT. Compos Struct 2013;105:369–84.
[72] Batra RC, Xiao J. Finite deformations of full Sine-wave St.-Venant beam due to tangential and normal distributed loads using nonlinear TSNDT. Meccanica 2015;50:355–65.